NUMERICAL INVESTIGATION OF LANDSLIDE-TSUNAMI PROPAGATION AND TRANSFORMATION IN A WIDE SPECTRUM OF WATER BODY GEOMETRIES

GIOELE RUFFINI [(1)], VALENTIN HELLER [(2)] & RICCARDO BRIGANTI [(3)]

[(1,2,3)] Environmental Fluid Mechanics and Geoprocesses Research Group, Faculty of Engineering, University of Nottingham, Nottingham, UK
Gioele.ruffini1@nottingham.ac.uk; Valentin.heller@nottingham.ac.uk; Riccardo.briganti@nottingham.ac.uk

ABSTRACT

Large landslide-tsunamis are caused by mass movements such as landslides and rock falls impacting into a water body. Landslide-tsunami research is essentially based on the two idealised water body geometries (i) wave flume (2D, laterally confined wave propagation) and (ii) wave basin (3D, unconfined wave propagation). The wave heights in 2D and 3D vary by over one order of magnitude in the far field and the wave characteristics in intermediate geometries are currently not well understood. This article focuses on numerical landslide-tsunami propagation in the far field to quantify the effect of the water body geometry. The wave model SWASH, based on the non-hydrostatic non-linear shallow water equations, is used to simulate Stokes and solitary waves in 6 different idealised water body geometries. This includes 2D, 3D as well as intermediate geometries consisting of "channels" with diverging side walls. The wavefront length was found to be an excellent parameter to correlate the wave decay along the slide axis in all these geometries in agreement with Green's law. Semi-theoretical equations to predict the wave magnitude of the idealised waves in any desired point of the water bodies are also presented. The findings herein significantly improve the reliability of preliminary landslide-tsunami hazard assessment in water body geometries between 2D and 3D, as demonstrated with the application on the 2014 landslide-tsunami event in Lake Askja.

Keywords: Landslide-tsunamis, nonlinear waves, SWASH, solitary waves, wave propagation

1 INTRODUCTION

Tsunamis generated by landslides are a serious hazard in reservoirs (Panizzo et al., 2005), lakes (Gylfadóttir et al., 2017), fjords (Harbitz et al., 2014) and the sea (Watt et al., 2012). In this work the term "landslide" applies to mass movements such as unstable soil, rock falls, calving icebergs and snow avalanches and the term "tsunami" specifies (low frequency) waves in water bodies such as lakes, reservoirs, fjords and the sea. One of the most destructive recorded landslide-tsunami was caused by an approximately 270×10^6 m^3 large landslide impacting into the Vajont reservoir in Italy in 1963. The generated wave overtopped the dam crest and flooded the valley resulting in approximately 2000 casualties (Panizzo et al., 2005). Potential landslide-tsunamis need to be assessed quite frequently on a global scale considering regions such as China with over 87000 reservoirs (Liu et al., 2013), Norway with 1190 fjords (Wikipedia, 2019) and many new projects to build hydropower reservoirs. This highlights the need for reliable landslide-tsunami hazard assessment methods.

Landslide-tsunamis are most reliably investigated in case specific water bodies given that the geometry and bathymetry may significantly affect the wave characteristics (Heller et al., 2012; Winckler and Liu, 2015). For generic studies, however, it is common practice to use idealised geometries. These are flume geometries (2D) and rarer basin geometries (3D), both with a uniform water depth. Despite such large idealisations, these geometries can indeed be found in nature with examples shown in Fig. 1. In a 2D geometry the wave propagates in the length direction of the water body with the coordinate x from the landslide impact and with the water body side angles $\theta = 0°$ (Fig. 1a). In a 3D geometry the waves propagate with semi-circular fronts defined with the radial distance r and a propagation angle γ from the slide impact with $\theta = 90°$ (Fig. 1b).

Wave decay with distance from the landslide impact zone has been studied extensively in both 2D and 3D revealing very different behaviours. For 2D geometries, theoretical and laboratory studies showed decay rates that are much lower (Heller and Spinneken, 2013) than in 3D (Panizzo et al., 2005; Evers et al., 2019). These studies indicate an order of magnitude difference in the wave height between 2D and 3D at the same location in the far field which was experimentally confirmed by Heller and Spinneken (2015). These authors also found that the landslide-tsunami wave type changes in function of the geometry. While in 2D tsunamis are commonly linked to the theoretical Stokes, cnoidal, solitary waves and bores (Heller and Hager, 2011) only the least nonlinear Stokes and cnoidal waves are observed in 3D.

Figure 1. Landslide-tsunami settings represented by idealised geometries: (a) Helheim Glacier representing a 2D geometry (contains modified Copernicus Sentinel data, 2016, processed by Pierre Markuse) and (b) 2007 Chehalis lake case representing a 3D geometry (adapted from Google maps).

Most studies involving the effect of the water body geometry were aimed at relating landslide-tsunami parameters in 3D to 2D (Heller et al., 2009; Heller and Spinneken, 2015). Since these studies commonly focus on 2D and/or 3D only, the understanding of landslide-tsunamis in intermediate geometries is limited. The pioneer study investigating an intermediate geometry was Chang et al. (1979) generating solitary waves in a flume with walls at an angle of θ = 1.1°. They found that Green's law can be applied for $x/h < 40$ where h is the water depth. However, Green's law was found to have limited applicability for solitary and solitary-like waves for more extremely diverging flumes (Heller et al., 2012), if the width of the diverging channel is used in Green's law. Heller et al. (2012) experimentally investigated for the first time landslide-tsunamis in different water body geometries with θ = 0 (2D), 15, 30, 45, 60, 75 and 90° (3D). They found that the wave heights in the far field in intermediate geometries were closer to the ones observed in 3D than in 2D. Heller and Spinneken (2015) conducted laboratory experiments in 2D and 3D with tsunamis measured up to a distance of $x/h = r/h = 35$. Intermediate geometries with θ = 7.5, 15, 30 and 45° were then numerically addressed with Smoothed Particle Hydrodynamics (SPH) (Heller et al., 2016). However, the distances were limited to $r/h \leq 7.5$ due to the high computational cost of the model.

Subaerial landslide-tsunamis are a major challenge for numerical modelling. The wave generation and wave propagation processes are usually simulated separately by coupling two different numerical models (Abadie et al., 2012; Altomare et al., 2015; Tan et al., 2018). The wave generation zone, with coordinate system x and (r, γ) from the slide impact, is the zone where the momentum transfer between the landslide and water occurs (Zitti et al., 2016). This zone is excluded from the present study ensuring that the tsunamis are reasonably stable in the simulations.

This study numerically addresses landslide-tsunami propagation using SWASH, based on the Non-hydrostatic Non-Linear Shallow Water Equations (NLSWEs). The aim is to enhance the physical understanding and modelling of the effect of the water body geometry on tsunami propagation and provide new semi-theoretical equations accounting of the effect of the water body geometry to support landslide-tsunami hazard assessment. SWASH is able to consider frequency dispersion accurately with a small number of layers (e.g. 2) by using a compact difference scheme, and can be run in parallel. Only idealised wave trains rather than wave packets are simulated as this is more similar to actual tsunami propagation and it avoids spurious numerical solutions due to propagation of isolated waves or packets in still water.

2 METHODOLOGY

2.1 Numerical setup

SWASH v4.01 (Zijlema et al., 2011) is used in the present study with a set of numerical domains that cover the range from 2D to 3D (Fig. 2). The 2D geometry consists of a 28.3 m long and 0.6 m wide flume while the 3D geometry (Fig. 2) spans a domain of 28.3 m × 64.0 m. Intermediate geometries are defined using divergent side walls with angles of θ = 7.5, 15, 30 and 45° (Fig. 2). Geometries with θ > 45° were excluded as previous research (Heller et al., 2012; 2016) showed no substantial differences of the maximum wave parameters in these geometries relative to the 3D case. The width of these intermediate geometries is increasing with $0.6 + 2r'\tan\theta$ m. Each intermediate geometry has been modelled with a rounded downwave boundary with radius r' = 28.3 m to allow for a more even distribution of the cells in this zone. The bathymetry was flat for all investigated cases and numerical wave gauges were placed at the locations shown in Table 1.

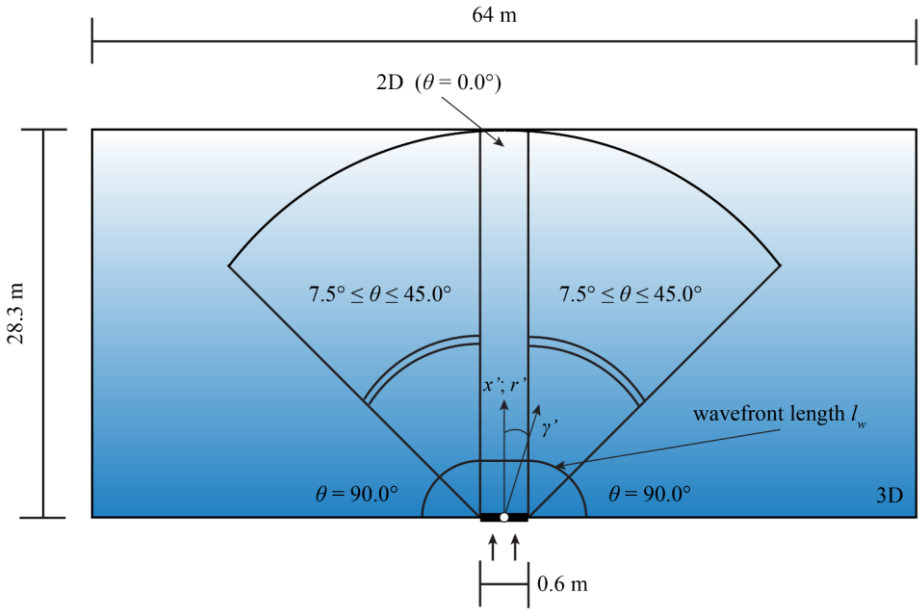

Figure 2. Investigated water body geometries in SWASH: 2D (θ = 0.0°), θ = 7.5, 15, 30, 45° and 3D (θ = 90.0°).

For the 2D and 3D geometries, the simulations are directly solved with a Cartesian coordinate system. For the intermediate geometries, orthogonal curvilinear grids are generated using RGFGRID v5.0 and imported in SWASH. The origin in the y'-direction is defined at the centre of the wave source which is 0.6 m wide in all domains. The results, in contrast to the calculations, are presented in polar coordinates (r', γ') with the origin at the centre of the wave source, with r' as the radial distance and γ' as the wave propagation angle with the results interpolated from the grid nodes. Note that the apostrophe indicates the coordinates of the wave propagation zone where $x' = x + d_M$ (2D) and $r' = r + d_M$ (3D) with the origins located at the coupling location at a distance d_M from the impact of the slide.

The Intel-MPI libraries, relying on the Message Passing Interface (MPI) protocol for the use of multiple processors, together with a stripwise decomposition method along the y'-axis, have been employed for the simulations on the University of Nottingham High Performance Computing (HPC) clusters Minerva and Augusta.

Table 1. Locations of the numerical wave gauges.

Geometry	Relative distance x'/h or r'/h (-)	Wave propagation angle γ' (°)
2D	3.0, 5.0, 7.5, 10.0, 15.0, 22.5, 35.0	0.0°
7.5°	3.0, 5.0, 7.5, 10.0, 15.0, 22.5, 35.0	0.0°, ±7.5°
15.0°	3.0, 5.0, 7.5, 10.0, 15.0, 22.5, 35.0	0.0°, ±7.5°, ±15.0°
30.0°	3.0, 5.0, 7.5, 10.0, 15.0, 22.5, 35.0	0.0°, ±7.5°, ±15.0°, ±22.5°, ±30.0°
45.0°	3.0, 5.0, 7.5, 10.0, 15.0, 22.5, 35.0	0.0°, ±7.5°, ±15.0°, ±22.5°, ±30.0°, ±37.5° ±45.0°
3D	3.0, 5.0, 7.5, 10.0, 15.0, 22.5, 35.0	0.0°, ±7.5°, ±15.0°, ±22.5°, ±30.0°, ±37.5° ±45.0°, ±52.5°, ±60.0°, ±67.5°, ±75.0°, ±82.5°

2.2 Boundary conditions

Previous studies (e.g. Heller and Hager, 2011) showed that different slide scenarios lead to different wave types and decay characteristics. Two of these wave types namely Stokes (Fenton, 1985) and solitary waves (Boussinesq, 1872) are reproduced herein. The conditions for each wave type presented in Figs. 4 (Stokes-like waves) and 8 (solitary-like waves) of Heller and Hager (2011) are reproduced by using the measured wave parameters in the corresponding wave theory. A time series of the water surface is calculated for each wave type and used as input for SWASH over a finite wave generation boundary $b' = 0.6$ m. The wave velocity is not included in the input but solved directly by SWASH as previous work showed the accuracy of this approach (Ruffini et al., 2019a). A ramping up function is also added for the Stokes waves to smooth the initiation of the simulations and avoid numerical instabilities. The used wave parameters are summarised in Table 2 with a as the amplitude, c as the celerity, L as the wavelength and T as the wave period. The first waves in the simulations of the Stokes waves are disregarded in the analysis to include only steady wave heights.

Table 2. Wave theories used in this study with the wave parameters measured in Heller and Hager (2011).

Wave theory	h (m)	H (m)	T (s)	L (m)	a (m)	c (m/s)
5th order Stokes (Fenton, 1985)	0.600	0.100	1.000	1.530	-	-
1st order solitary (Boussinesq, 1872)	0.300	0.159	-	2.823	0.159	1.969

The wave generation boundary is defined through a segment at x' = 0 m using a weakly reflective boundary condition (Blayo and Debreu, 2005). In addition, all the lateral walls are represented by closed boundaries with zero flux velocity (Stelling and Zijlema, 2003). To avoid wave reflection from the downwave end of the domain, a sponge layer (Dingemans, 1997) with a length of at least 3 times L was used in all geometries. Two additional lateral sponge layers were used in the 3D geometry to allow the analysis of the lateral energy spread without reflections from the lateral walls. Finally, for the bottom friction a formulation based on Manning's roughness coefficient where n = 0.009 s/m$^{1/3}$ for glass is used to mimic the 2D experimental conditions in Heller and Hager (2011).

2.3 Calibration

The grids follow the Deltares (2019) guidelines with respect to orthogonality, smoothness, aspect ratio and minimum number of grid points per wavelength. The number of grid points per wavelength is set to at least 45. This is a finer resolution than in van Vledder and Zijlema (2014) who used 25 grid points per wavelength resulting in good agreement with theory in SWASH for diffraction at a semi-infinite breakwater. In addition, a higher order discretisation scheme, compared to the default scheme in SWASH, has been used to Stokes waves. This was necessary to avoid excessive numerical dissipation, observed for the default scheme, particularly in 2D, associated with the higher harmonics used in that particular case (SWASH, 2016). This dissipation was not observed for the solitary wave case.

The 3D geometry is used to investigate the convergence for $\Delta x'$ = $\Delta y'$ = 2.5, 5.0 and 10.0 cm and the symmetry of the solution (Ruffini et al., 2019b). Convergence of the solution was found for 5.0 cm, however, the final resolution was set to 2.5 cm to also satisfy the minimum value of grid points per L. SWASH matches higher order dispersion relations depending on the number of layers over the water depth. Higher values of kh, with k as the wave number, require a larger number of layers which shows indirectly the importance of wave dispersion for different kh values. Herein, 2 layers are chosen which results in a maximum error of 1% with $kh \leq 7.7$ (SWASH team, 2016).

3 RESULTS

3.1 Wave height decay

To investigate the wave decay, H is calculated from the water surface η time series (and averaged over 5T for the Stokes waves). Values were calculated for both wave types and all geometries at the locations shown in Table 1. Fig. 3 shows H/h over the relative distance r'/h for each geometry for $\gamma' = 0°$. This clearly confirms the increasing decay of H with θ. Fig. 3a show differences of a factor of 3.0 between the 2D and $\theta = 7.5°$ geometry and 7.9 between 2D and 3D at $r'/h = 35$. For the solitary waves (Fig. 3b) the decay is slightly lower with differences of a factor of 2.9 and 8.4 between the same geometries matching the results of Heller and Spinneken (2015).

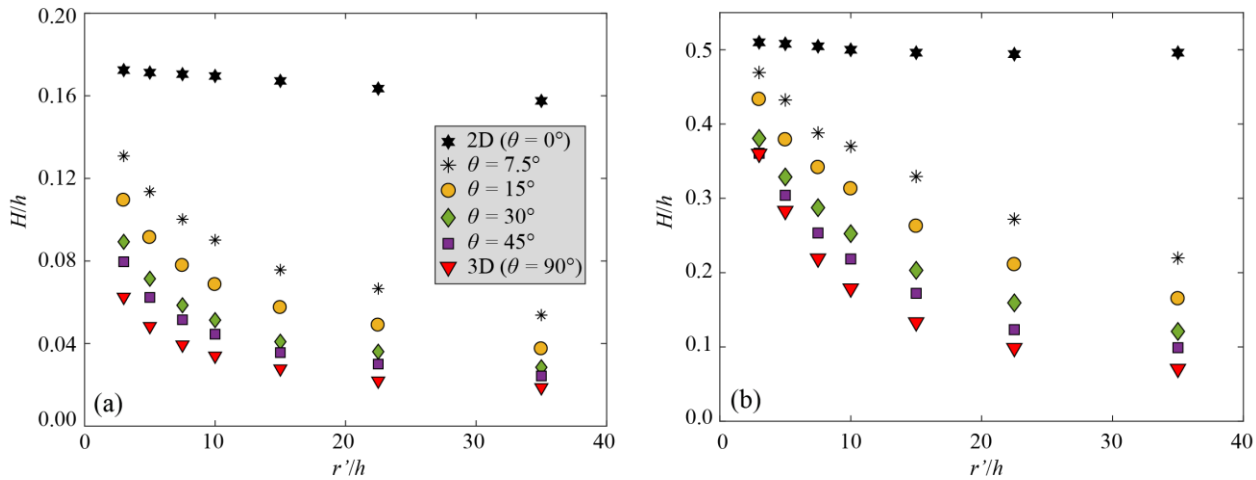

Figure 3. Relative wave height H/h decay with relative distance r'/h for different water body geometries for (a) 5th order Stokes waves and (b) 1st order solitary waves.

The wavefront length l_w (Fig. 2) was identified as an excellent parameter to link the wave decay of the idealised waves across all water body geometries. The waves propagate with circular arc fronts from the source and if the source width b' is relatively small, it can also be approximated as a line. The values of l_w are then calculated for the numerical results as

$$l_w(r', \theta) = b' + 2r'\theta_{rad} \quad [1]$$

where r' is the radial distance and θ_{rad} the water body side angle in radians. This parameter l_w normalised with the water depth h (i.e. l_w/h) is used to correlate H/h for both idealised wave types in Fig. 4 where different geometries are highlighted with different markers. Green's law is included as

$$H(r', \theta) = H(r' = 0, \theta = 0°) \left(\frac{b'}{l_w(r', \theta)}\right)^{1/2} \left(\frac{h(r' = 0)}{h(r')}\right)^{1/2}, \quad [2]$$

where $H(r', \theta)$ is the wave height in function of r' and θ, $l_w(r', \theta)$ and $h(r')$ are the associated wavefront length and water depth, respectively. $H(r' = 0, \theta = 0°)$ is the wave height at the source in 2D and b' is the source width. In the idealised geometries $h(r')$ is constant, such that the last term on the right-hand side of Eq. [2] reduces to 1. This equation can readily be applied by known wave characteristics at the source in 2D from a 2D study such as Heller and Hager (2010). The results for each wave type are then tested with the normalised Root Mean Square Error

$$nRMSE = \frac{\sqrt{\frac{1}{\mathrm{N}}\sum_{\mathrm{i}}^{\mathrm{N}}\left(y_{pred,\mathrm{i}} - y_{num,\mathrm{i}}\right)^2}}{\left(y_{num,max} - y_{num,min}\right)}, \quad [3]$$

where $y_{pred,\mathrm{i}}$ is the ith sample of the predicted parameter and $y_{num,\mathrm{i}}$ is the corresponding numerical value. N is the number of considered samples, $y_{num,max}$ and $y_{num,min}$ are respectively the maximum and the minimum numerical values in the range considered. $nRMSE$ = 0 represents perfect agreement.

Fig. 4a shows the results for the 5th order Stokes waves with a good agreement with Green's law (Eq. [2]). Fig. 4b shows the wave decay for solitary waves. The data scatter relative to Green's law in the range 6 < l_w/h < 40 is larger than for Stokes waves. For l_w/h < 6 and l_w/h > 40 there is still a close match between the data and Eq. [2]. The largest difference from Green's law is found for the 3D geometry with up to 40% difference in relative wave height.

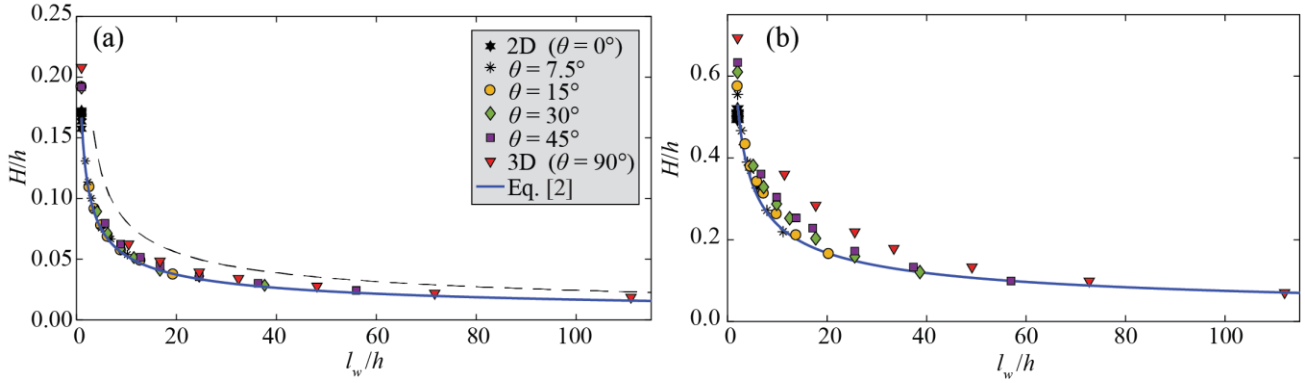

Figure 4. Relative wave height H/h decay with l_w/h for all investigated geometries for (a) 5th order Stokes waves and (b) 1st order solitary waves. The data are compared with Eq. [2] based on Green's law resulting in (a) $nRMSE$ = 0.06 and (b) $nRMSE$ = 0.08.

3.2 Lateral wave energy spread

In this section the lateral wave energy spread for both wave types is investigated. The wave height is calculated with a resolution of $\Delta\gamma'$ = 7.5° at different r'/h. Fig. 5 show the spatial distribution of the wave height for the 5th order Stokes waves with different r'/h values represented by different grey shades. The lateral wave decay becomes important with increasing θ. In the 3D geometry (Fig. 5f) the maximum wave heights at $\gamma' = 0°$ is found to be 20 - 34% larger than at γ'= ±82.5°.

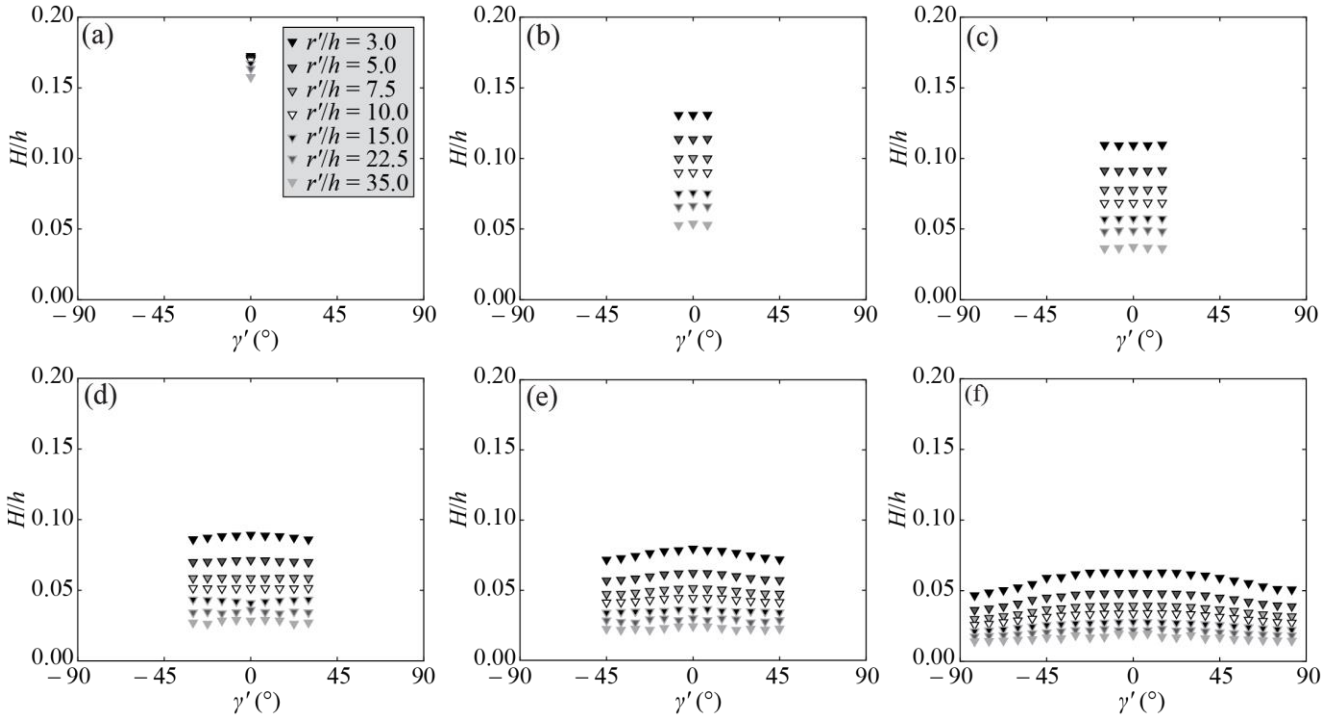

Figure 5. Relative wave heights H/h for Stokes waves as a function of the relative radial distance r'/h and the propagation angle γ' for (a) 2D (θ = 0°), (b) θ = 7.5°, (c) θ = 15°, (d) θ = 30°, (e) θ = 45° and (f) 3D (θ = 90°).

Fig. 6 shows H normalised by using Eq. [2], on the y-axis, over the wave propagation angle γ' for all simulated wave geometries. Green's law is reduced to a blue circle. The lateral wave energy spread is represented by the term $\cos^2(\gamma'/3)$. This term is inspired by Heller and Spinneken (2015) and Huber and Hager (1997) who found $\cos^{2\{1+\exp[-0.2(r/h)]\}}(2\gamma/3)$ and $\cos^2(2\gamma/3)$, respectively, for experimental data based on the 3D geometry. The value 2/3 is reduced to 1/3 herein. This smaller lateral wave decay is associated with the lack of slide momentum in the far field, where the present results apply, in contrast to Heller and Spinneken (2015) and Huber and Hager (1997) involving also the near field with a larger lateral decay. To reproduce the lateral decay trend in the far field, the empirical term $\cos^2(\gamma'/3)$ is added to the theoretical Eq. [2] resulting in

$$\frac{H(r',\gamma',\theta)}{h} \Big/ \left(\frac{b'}{l_w(r',\theta)}\right)^{1/2} = \beta \frac{H(r'=0,\gamma'=0,\theta=0°)}{h} \cos^2\left(\frac{\gamma'}{3}\right) \qquad [4]$$

where $H(r',\gamma',\theta)$ is the wave height at the position r' and γ', $l_w(r',\theta)$ is the corresponding wavefront length and $H(r'=0,\gamma'=0,\theta=0°)$ is the incident 2D wave height.

A similar expression is obtained for the linear wave amplitude a by replacing H in Eq. [4] resulting in

$$\frac{a(r',\gamma',\theta)}{h} \Big/ \left(\frac{b'}{l_w(r',\theta)}\right)^{1/2} = \beta \frac{a(r'=0,\gamma'=0,\theta=0°)}{h} \cos^2\left(\frac{\gamma'}{3}\right) \qquad [5]$$

Note that Eq. [5] will be applied to non-linear waves as a simplification hereafter. h = constant is maintained in Eqs. [4] and [5] to keep the equations in dimensionless form. The empirical pre-factor β is applied to $H(r'=0,\gamma'=0,\theta=0°)$ and $a(r'=0,\gamma'=0,\theta=0°)$ to determine the upper envelope (β_E) and the best overall fit (β) of the numerical data. β is based on the smallest $nRMSE$, which together with the corresponding ±% scatter is summarised in Table 3 for both H and a.

The black curve in Fig. 6 represents Eq. [4] with β = 1, the red line with β_E and the dashed line with β. Stokes waves result in the smallest β_E = 1.25 for H requiring only 25% increase from the semi-theoretical expression to reach the upper envelope. The best fit is achieved with β = 1.10 with a data scatter of +13% and −14%. The solitary waves (Fig. 6b) result in a larger difference between the black and the red curves with β_E = 1.61 and β = 1.20 with a data scatter of +36% and −21%. For the solitary wave the black curve corresponds simultaneously to a lower envelope of the values. This is already indicated in Fig. 4b where all points lay above Green's law. For Stokes waves the best fit of the wave amplitude a is achieved for β >1 and β_E > 1, while for the solitary waves β < 1 and β_E > 1 as shown in Table 3.

Fig. 6 allows for a semi-theoretical prediction of idealised tsunami heights for both investigated wave types, all geometries and locations. These predictions take the effect of the water body geometry into account as well as bottom friction. However, they are based on idealised wave types which, unlike real tsunamis, are not affected by (i) the bathymetry due to a constant water depth and (ii) frequency dispersion (Ruffini et al., 2019b).

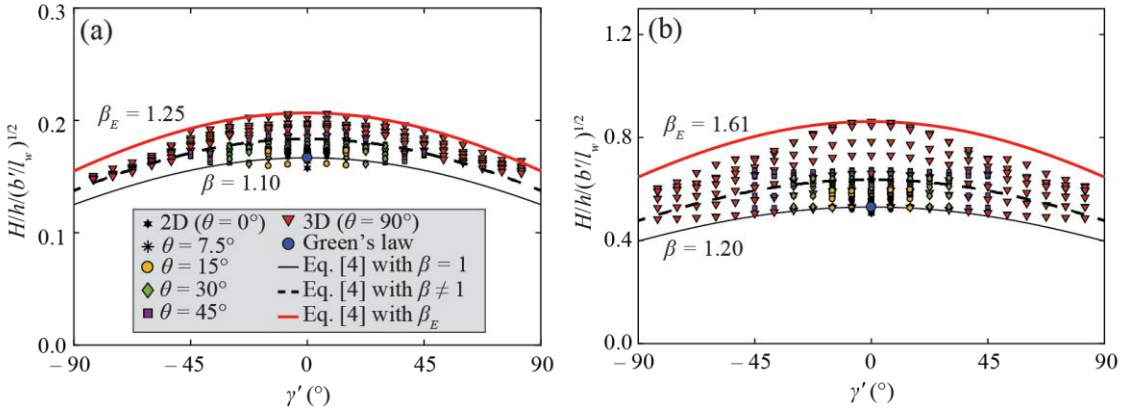

Figure 6. Relative lateral wave decay for all investigated geometries compared to Eq. [4] for (a) 5th order Stokes waves and (b) 1st order solitary waves.

Table 3. Pre-factors for wave height H (Eq. [4]) and wave amplitude a (Eq. [5]) for both investigated wave types. The upper envelope is determined with β_E and the best overall fit with β.

Wave theory		***H***			***a***	
	β_E	β $(nRMSE)$	±scatter	β_E	β $(nRMSE)$	±scatter
5th order Stokes	1.25	1.10 (0.17)	+13%, –14%	1.18	1.01 (0.14)	+17%, –14%
1st order solitary	1.61	1.20 (0.21)	+36%, –21%	1.14	0.84 (0.23)	+36%, –38%

4 DISCUSSION

4.1 Computation example

A procedure to predict landslide-tsunamis using Eqs. [4] and [5] is presented hereafter. The present study only addresses wave propagation, while already available relationships for the 2D case from Heller and Hager (2010) allow to compute the maximum wave height and its position for granular slides in the wave generation zone. The slide width b' at the coupling location is approximated with the slide width b from the impact zone plus an arc section on either side of the slide (Fig. 7). This approximation is necessary as a straight line at the coupling location would converge to infinity with increasing θ. This approximation satisfies the energy conservation between $l_w(r' = 0, \theta)$ and $l_w(r', \theta)$, which coincides with the assumptions made for Green's law. The application procedure of Eq. [4] can be summarised with the following steps:

1. Define the landslide width b, thickness s, mass m_s, impact velocity V_s, slope angle α, density ρ_s, water density ρ_w and water depth h
2. Evaluate the wave type in 2D using the wave type product T of Heller and Hager (2011)
3. Calculate the maximum wave height for 2D and its position from the slide impact $r = d_M$
4. Define θ_1 and θ_2 (Fig. 7) at the slide sides to approximate the current geometry to an idealised one up to $r' = 0$ and calculate the wave front length $l_w(r' = 0, \theta)$
5. Compute $H(r' = 0, \gamma' = 0, \theta)$ by applying energy conservation

$$H(r' = 0, \gamma' = 0, \theta) = H_M(r' = 0, \gamma' = 0, \theta = 0°)\,[b'/l_w(r' = 0, \theta)]^{1/2} \qquad [6]$$

6. Define θ_3 and θ_4 (Fig. 7) at the slide sides to approximate the geometry up to a desired distance $r' > 0$, thereby taking any restrictions or expansions of the water body into account, and calculate $l_w(r', \theta)$
7. Use Eq. [4] to calculate $H(r', \gamma', \theta)$ at the desired location.

These steps are illustrated with the 2014 Lake Askja landslide-tsunami event in Iceland. The wave heights are computed at one position and compared with the numerical results of Gylfadóttir et al. (2017). The slide parameters are defined first as shown in Table 4 (step 1).

The wave type product $\mathrm{T} = S^{1/3} M \cos(6/7\alpha) = 1.21$ (Table 4), with $S = 0.26$ and $M = 1.91$, is calculated to evaluate the wave type (step 2). This product T for granular landslides is in the range of $4/5\mathrm{F}^{-7/5} \leq \mathrm{T} \leq 11\mathrm{F}^{-5/2}$ (1.06 ≤ 1.21 ≤ 18.06) for which cnoidal and solitary-like waves are expected in 2D (Heller and Hager, 2011).

The former wave type was chosen because T is closer to the lower boundary of the range where less energetic waves are expected. As cnoidal waves were not investigate herein, the values from Ruffini et al. (2019b), who found β = 1.03 and β_E = 1.27, are used.

Table 4. Dimensional and non-dimensional landslide parameters and wave characteristics for the 2014 Lake Askja landslide-tsunami.

b (m)	s (m)	α (°)	V_s (m/s)	m_s (kg)	ρ_s (kg/m³)	ρ_w (kg/m³)	h (m)
550.0	35.5	10.4	30.1	2 ×10¹⁰	2000	1000	138.0
S (-)	**M (-)**	**F (-)**	**T (-)**	**P (-)**	**d_M (m)**	**H_M (m)**	**a_M (m)**
0.26	1.91	0.82	1.21	0.49	531	43.3	34.7

The maximum wave height H_M is computed with $H_M = 5/9\mathrm{P}^{4/5}h$ (Table 5) (Heller and Hager, 2010) for 2D with the impulse product parameter $\mathrm{P} = \mathrm{F}S^{1/2}M^{1/4}\{\cos[(6/7)\alpha]\}^{1/2}$ (step 3). Because the geometry of the Lake Askja is not symmetrical, different θ were selected on the two slide sides. The wavefront length at $r = d_M$ is thus calculated using θ_1 = 32.4°, θ_2 = 44.1° (Fig. 7) and the slide width b = 550 m resulting in $l_w(r = d_M, \theta) = b + \theta_{rad,1}d_M + \theta_{rad,2}d_M = 550 + 32.4(\pi/180)531 + 44.1(\pi/180)531 = 1259$ m (step 4). Note that r' in Eq. [1] is replaced here with r because the geometry already starts to diverge at r = 0 rather than at r' = 0. Since H_M applies to 2D, the observed wave height at the coupling location is smaller due to lateral energy spread. This is taken into account by spreading the wave energy over the wavefront length resulting in $H(r' = 0, \gamma' = 0, \theta) = H_M(r' = 0, \gamma' = 0, \theta = 0°)[b'/l_w(r' = 0, \theta)]^{1/2} = 43.3(550/1259)^{1/2} = 28.6$ m (step 5).

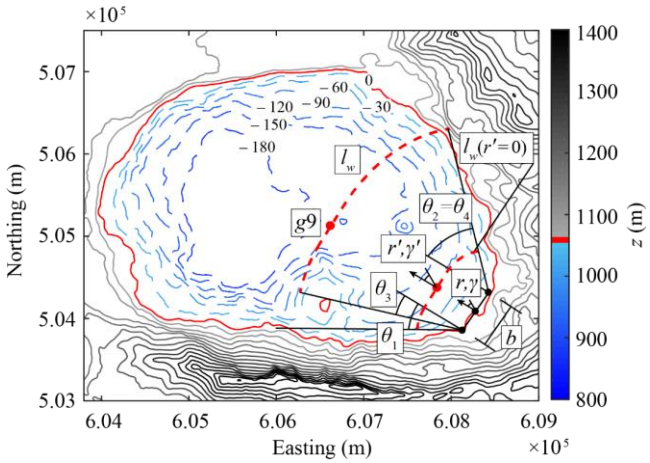

Figure 7. Computation example for wave gauge 9 of Gylfadóttir et al. (2017). Still water level SWL = 1058 m above sea level (red solid line). The contours represent a vertical terrain spacing of Δz = 30 m with dashed lines and solid lines representing the terrain elevation below and above the lake SWL, respectively.

The wave height is calculated at wave gauge 9 ($r = 1970$ m, $\gamma = 0°$) of Gylfadóttir et al. (2017). The wavefront length again with r' replaced by r, is $l_w = 550 + 19.2(\pi/180)1970 + 44.1(\pi/180)1970 = 2726$ m by using θ_3 = 19.2° and θ_4 = 44.1° (Fig. 7, step 6). θ_3 is chosen under the consideration of the water body restriction caused by the small island on the left-hand side of the slide, which affects the lateral wave energy spread. Finally, applying Eq. [4] for $\gamma = 0°$ with the pre-factor for the best fit β = 1.03 (Table 3 in Ruffini et al., 2019b) results in $H = 1.03[28.6(1259/2726)^{1/2}] = 20.0$ m (step 7). This value is close (−10.0%) to the wave height H = 22.2 m found by Gylfadóttir et al. (2017).

The same procedure can be applied to calculate a using Eq. [5] with $\beta = 0.85$ (Ruffini et al., 2019b) and defining the maximum wave amplitude in 2D as $a_M = 4/9\mathrm{P}^{4/5}h$ from Heller and Hager (2010) (Table 4) resulting in a = 13.2 m (−1.5%) at gauge 9 compared to a = 13.4 m found by Gylfadóttir et al. (2017).

5 CONCLUSIONS

This study aimed to enhance the physical understanding of the effect of the water body geometry on landslide-tsunami propagation. This aim was motivated by the very limited understanding of this effect for intermediate geometries between the 2D (flume) and 3D (basin) geometries.

Idealised water body geometries with increasing side angle $\theta = 0$ (2D), 7.5, 15, 30, 45 and 90° (3D) of the flume lateral walls were used to simulate idealised landslide-tsunamis. The non-hydrostatic non-linear shallow water equations model SWASH was used to simulate tsunami propagation in the far field, where the wave is

reasonably stable. Stokes and solitary waves were investigated up to a maximum distance of 35 times the water depth from the wave generation zone. The wavefront length l_w (Eq. [1]) was found to link the wave heights of the idealised waves in all investigated geometries along the slide axis with a close agreement with Green's law (Eq. [2]). The wave heights off the slide axes were also correlated with Green's law, modified with empirical pre-terms. The derived semi-theoretical equations can be used to predict the wave heights and amplitudes in real water bodies, directly based on the wave parameters from 2D of Heller and Hager (2010). Finally, a calculation procedure to apply the new semi-theoretical equations to the real Lake Askja tsunami in 2014 was provided showing a good agreement of the wave heights (−10.0%) and amplitudes (−1.5%).

This work addressed idealised waves essentially excluding frequency dispersion. The decay in 2D for landslide-tsunamis is mainly caused by frequency dispersion if bottom friction is excluded. For more diverging geometries the additional contribution of lateral energy spread is also present. However, due to the non-linearity of the problem it is not possible to separate the two contributions frequency dispersion and lateral energy spread for these cases. Ruffini et al. (2019b) investigated the effect of frequency dispersion in 2D showing that it may be neglected for tsunamis in proximity of the shallow-water wave regime (solitary-like waves), however, in proximity of the deep-water wave regime (Stokes-like waves) frequency dispersion becomes more relevant and cannot be neglected. The new equations can then still be applied within initial landslide-tsunami hazard assessments, but will likely result in an over-prediction of real waves and operate on the safe side. Future work will investigate the effect of the bathymetry on tsunamis with the aim to combine the effects of the geometry and bathymetry.

ACKNOWLEDGEMENTS

The authors would like to thank Prof Nicholas Dodd for helpful suggestions for this work. Dr Sigríður Sif Gylfadóttir and her collaborators are acknowledged for providing their numerical results for the Lake Askja case. The University of Nottingham HPC clusters Minerva and Augusta were accessed to perform the numerical simulations.

REFERENCES

Abadie, S.M., Harris, J.C., Grilli, S.T. and Fabre, R. (2012). Numerical modeling of tsunami waves generated by the flank collapse of the Cumbre Vieja Volcano (La Palma, Canary Islands): Tsunami source and near field effects. *Journal of Geophysical Research: Oceans* 117(C05030).

Altomare, C., Domínguez, J.M., Crespo, A.J.C., Suzuki, T., Caceres, I. and Gómez-Gesteira, M. (2015). Hybridization of the wave propagation model SWASH and the mesh free particle method SPH for real coastal applications. *Coastal Engineering Journal* 57(4), 1-34.

Blayo, E. and Debreu, L. (2005). Revisiting open boundary conditions from the point of view of characteristic variables. *Ocean Modelling* 9(3), 231–252.

Boussinesq, J. (1872). Théorie des ondes et des remous qui se propagent le long d'un canal rectangulaire horizontal, en communiquant an liquide contenu dans ce canal de vitesses sensiblement pareilles de la surface anfond, liouvilles. *Journal de Mathématiques Pures et Appliquées* 17, 55–108.

Chang, P., Melville, W.K. and Miles, J.W. (1979). On the evolution of a solitary wave in a gradually varying channel. *Journal of Fluid Mechanics* 95(3), 401–414.

Deltares (2019). *Delft 3D modelling guidelines*. URL: https://publicwiki.deltares.nl/display/D3DGUIDE/Computational+grid (accessed 21/05/2019).

Dingemans, M.W. (1997). *Water wave propagation over uneven bottoms: Part 1*. World Scientific, Singapore.

Evers, F.M., Hager, W.H. and Boes, R.M. (2019). Spatial impulse wave generation and propagation. *Journal of Waterway, Port, Coastal, and Ocean Engineering* 145(3), 04019011, 1–15.

Fenton, J.D. (1985). A fifth-order Stokes theory for steady waves. *Journal of Waterway, Port, Coastal, and Ocean Engineering* 111(2), 216–234.

Gylfadóttir, S.S., Kim, J., Helgason, J.K., Brynjólfsson, S., Höskuldsson, Á., Jóhannesson, T., Harbitz, C.B. and Løvholt, F. (2017). The 2014 Lake Askja rockslide induced tsunami: Optimization of numerical tsunami model using observed data. *Journal of Geophysical Research: Oceans* 122(5), 4110–4122.

Harbitz, C.B., Glimsdal, S., Løvholt, F., Kveldsvik, V., Pedersen, G.K. and Jensen, A. (2014). Rockslide tsunamis in complex fjords: From an unstable rock slope at Åkerneset to tsunami risk in western Norway. *Coastal Engineering* 88, 101–122.

Heller, V., Bruggemann, M., Spinneken, J. and Rogers, B.D. (2016). Composite modelling of subaerial landslide-tsunamis in different water body geometries and novel insight into slide and wave kinematics. *Coastal Engineering* 109, 20–41.

Heller, V. and Hager, W.H. (2011). Wave types of landslide generated impulse waves. *Ocean Engineering* 38(4), 630–640.

Heller, V. and Hager, W.H. (2010). Impulse product parameter in landslide generated impulse waves. *Journal of Waterway, Port, Coastal, and Ocean Engineering* 136(3), 145–155.

Heller, V., Hager, W.H. and Minor, H.-E. (2009). Landslide generated impulse waves in reservoirs: Basics and computation. R. Boes, ed. ETH Zurich, Zurich.

Heller, V., Moalemi, M., Kinnear, R.D. and Adams, R.A. (2012). Geometrical effects on landslide-generated tsunamis. *Journal of Waterway, Port, Coastal, and Ocean Engineering* 138(4), 286–298.

Heller, V. and Spinneken, J. (2013). Improved landslide-tsunami prediction: Effects of block model parameters and slide model. *Journal of Geophysical Research: Oceans* 118(3), 1489–1507.

Heller, V. and Spinneken, J. (2015). On the effect of the water body geometry on landslide-tsunamis: Physical insight from laboratory tests and 2D to 3D wave parameter transformation. *Coastal Engineering* 104,113–134.

Huber, A. and Hager, W.H. (1997). Forecasting impulse waves in reservoirs, in: *Transactions of the International Congress on Large Dams* 1, Florence, 993–1006.

Liu, J., Zang, C., Tian, S., Liu, J., Yang, H., Jia, S., You, L., Liu, B. and Zhang, M. (2013). Water conservancy projects in China: Achievements, challenges and way forward. *Global Environmental Change* 23(3), 633–643.

Panizzo, A., Girolamo, P.D., Risio, M.D., Maistri, A. and Petaccia, A. (2005). Great landslide events in Italian artificial reservoirs. *Natural Hazards and Earth System Sciences* 5(5), 733–740.

Ruffini, G., Briganti, R., Alsina, J.M., Brocchini, M., Dodd, N. and McCall, R. (2019a). Numerical modelling of flow and bed evolution of bi-chromatic wave groups on an intermediate beach using non-hydrostatic Xbeach. *Journal of Waterway, Port, Coastal, and Ocean Engineering* (in press).

Ruffini, G., Heller, V. and Briganti, R. (2019b). Numerical modelling of landslide-tsunami propagation in a wide range of idealised water body geometries (in press).

Stelling, G. and Zijlema, M. (2003). An accurate and efficient finite-difference algorithm for non-hydrostatic free-surface flow with application to wave propagation. *International Journal for Numerical Methods in Fluids* 43(1), 1–23.

SWASH team (2016). *SWASH - User manual Version 4.01*. Delft University of Technology, Environmental Fluid Mechanics Section.

Tan, H., Ruffini, G., Heller, V. and Chen, S. (2018). A numerical landslide-tsunami hazard assessment technique applied on hypothetical scenarios at Es Vedrà, offshore Ibiza. *Journal of Marine Science and Engineering* 6(4), 1–22.

van Vledder, G.P. and Zijlema, M. (2014). Non-hydrostatic wave modeling in partly sheltered harbor basins. *Coastal Engineering Proceedings* 1(34), 1–11.

Watt, S.F.L., Talling, P.J., Vardy, M.E., Heller, V., Hühnerbach, V., Urlaub, M., Sarkar, S., Masson, D.G., Henstock, T.J., Minshull, T.A., Paulatto, M., Le Friant, A., Lebas, E., Berndt, C., Crutchley, G.J., Karstens, J., Stinton, A.J. and Maeno, F. (2012). Combinations of volcanic-flank and seafloor-sediment failure offshore Montserrat, and their implications for tsunami generation. *Earth and Planetary Science Letters* 319, 228–240.

Wikipedia (2019). URL: https://en.wikipedia.org/wiki/List_of_Norwegian_fjords (accessed 21/05/2019).

Winckler, P. and Liu, P.L.F. (2015). Long waves in a straight channel with non-uniform cross-section. *Journal of Fluid Mechanics* 770, 156–188.

Zijlema, M., Stelling, G. and Smit, P. (2011). SWASH: An operational public domain code for simulating wave fields and rapidly varied flows in coastal waters. *Coastal Engineering* 58(10), 992–1012.

Zitti, G., Ancey, C., Postacchini, M. and Brocchini, M. (2016). Impulse waves generated by snow avalanches: Momentum and energy transfer to a water body. *Journal of Geophysical Research: Earth Surface* 121(12), 2399–2423.